# Impedance Spectroscopy of Perovskite Solar Cells: Studying the Dynamics of Charge Carriers Before and After Continuous Operation

*Bekele Hailegnaw, Niyazi Serdar Sariciftci, and Markus Clark Scharber\**

The issue of long-term stability is one of the main obstacles challenging the progress of perovskite solar cells (PSCs). To alleviate this issue, a thorough understanding of the degradation mechanisms of the device is required. Herein, electrochemical impedance measurements in combination with maximum power point (MPP) tracking are applied to characterize PSCs, aiming to gain an understanding of the charge carrier dynamics in the photoactive bulk and at the contact-absorber-interfaces under operation. Electrochemical impedance spectroscopy (EIS) results show that the device charge transport resistance and interface capacitance associated with charge accumulation at the interfaces are both increasing upon continuous operation. This suggests ion migration from the photoactive perovskite layer to the charge transport layer interfaces leaving defects in the bulk. This suggests that reduction of the device performance upon continuous operation is mainly related to the changes in the bulk of the photoactive perovskite film and ions migration.

## 1. Introduction

Perovskite solar cells (PSCs) are one of swiftly evolving next-generation photovoltaic devices, which have attracted a lot of interest in the scientific community for the past 10 years. First devices with a power conversion efficiency (PCE) of about 3.8% were reported by Miyasaka and coworkers.[1] Since then, unprecedented improvements and breakthroughs in the PCE have been accomplished through extensive optimization of thin-film growth, careful interface designing, and compositional engineering. The current record PCE of PSC exceeds 25% which is comparable with crystalline silicon, cadmium telluride, and other high-performance solar cells.[2–5] However, long-term stability is one of the main issues challenging the process of

commercializing PSCs. The instability of PSCs is mainly originating from the degradation of the perovskite semiconductor as well as the degradation of the interfaces and electrode materials. There are both intrinsic and extrinsic factors affecting the stability of perovskites, for example, the exposure to ultraviolet (UV) light, sensitivity to moisture and oxygen, thermal instability, ion migration, or chemical instability.[6–9] Stability improvements have been achieved through compositional modification of the perovskite materials, structural modifications, and interfacial engineering of the perovskite layers.

Applying device encapsulation plays an important role to protect the hygroscopic photoactive layer from environmental moisture and oxygen.[7,10] Interface engineering by applying stabilizing layers such as hydrophobic inorganic and organic hole-transport and electron-transport layers (HTLs and ETLs), and engineering interfacial contacts can improve the lifetime of PSCs.[11–14] Using different cations has been shown to enhance the mechanical robustness, thermal, and moisture stability of the perovskite materials.[6,7,10,15,16]

The issue of ion migration is another factor affecting the device long-term stability which can be overcome using appropriate contacts and modifying the morphology and composition of the perovskite by alkali doping and replacement, multidimensional perovskites engineering, and applying molecular additives.[7,14,17]

A detailed understanding of the changes in the materials and the device structure and processes that occur in the devices under real-world conditions is required to alleviate the issues of stability. Many efforts have been devoted to this aspect in the past few years. Tress et al. studied the effect of light intensity and temperature on the PCE and long-term stability of PSCs under simulated ambient conditions and found reversible and irreversible degradation during the course of 1-year operation.[8] However, little is known about what happens inside the device structure causing the degradation upon continuous operation. The degradation of PSCs could originate from the degradation of the perovskite material, the interfacial materials, electrodes, or a combination of all.[18,19] To get insight into these issues, it is necessary to apply different characterization techniques that provide direct or indirect information about the degradation processes in the bulk, electrodes, and interfaces of the devices.

Dr. B. Hailegnaw, Prof. N. S. Sariciftci, Prof. M. C. Scharber
Linz Institute for Organic Solar Cells (LIOS)
Institute of Physical Chemistry
Johannes Kepler University Linz
Altenbergerstrasse 69, Linz 4040, Austria
E-mail: markus_clark.scharber@jku.at

In this work, we applied impedance spectroscopy techniques to study the electrical and ionic charge dynamics in the absorber layer as well as at the interfaces before and after continuous operation under simulated solar radiation. The goal of this investigation was to follow the changes in the electrochemical impedance spectroscopy (EIS) response of the PSCs and to identify the processes and mechanisms responsible for the reduction of device performance over time. PSCs with p-i-n device structure were fabricated. Devices were encapsulated and maximum power point (MPP)-tracking measurements were conducted for 48 h under AM1.5 (1 sun) illumination in ambient air. In parallel, the device photocurrent density–photovoltage ($J$–$V$) characteristic and electrochemical impedance responses were measured before and immediately after the MPP tracking. The electrical dynamics associated with the photoactive material confirms the increase in charge transport resistance and defect density in the bulk phase. The capacitive element associated with the ion accumulation at the interface confirms the ion migration to the interface. Further, a Mott–Schottky analysis of the device capacitance–voltage ($C$–$V$) response under dark conditions shows an increase in the trap density upon continuous operation.

## 2. Result and Discussion

To study the stability trend of $MAPbI_{3-x}Cl_x$ PSC under continuous operation, MPP tracking of four encapsulated PSCs was recorded in ambient air for 48 h. The device $J$–$V$ characteristics and electrical impedance spectroscopy (EIS) measurements were carried out before and after the MPP tracking.

The schematic diagram of the investigated device structure is shown in **Figure 1**a. The photocurrent density–voltage ($J$–$V$) characteristics (Figure 1b) show an increase in the device hysteresis and a decrease in the $V_{OC}$ and fill factor (FF), leading to an overall decrease in the PCE after continuous operation for 48 h. In addition, $J$–$V$ and impedance spectroscopy characterizations before and after continuous operation under MPP tracking were applied to devices with Bathocuproine (BCP) interlayer as a replacement for the $TiO_x$ interlayer with the objective to compare the device behavior under continuous operation. Device illustrates analogous photovoltaic characteristics with substantial decrease in the devices FF and PCE (see Figure S1a, Supporting Information). Figure 1c shows the MPP-tracking characteristics, the PCE and current density at MPP ($J_{max}$) of an encapsulated PSC under 1 sun light illumination in ambient air. The evolution of maximum power output and the
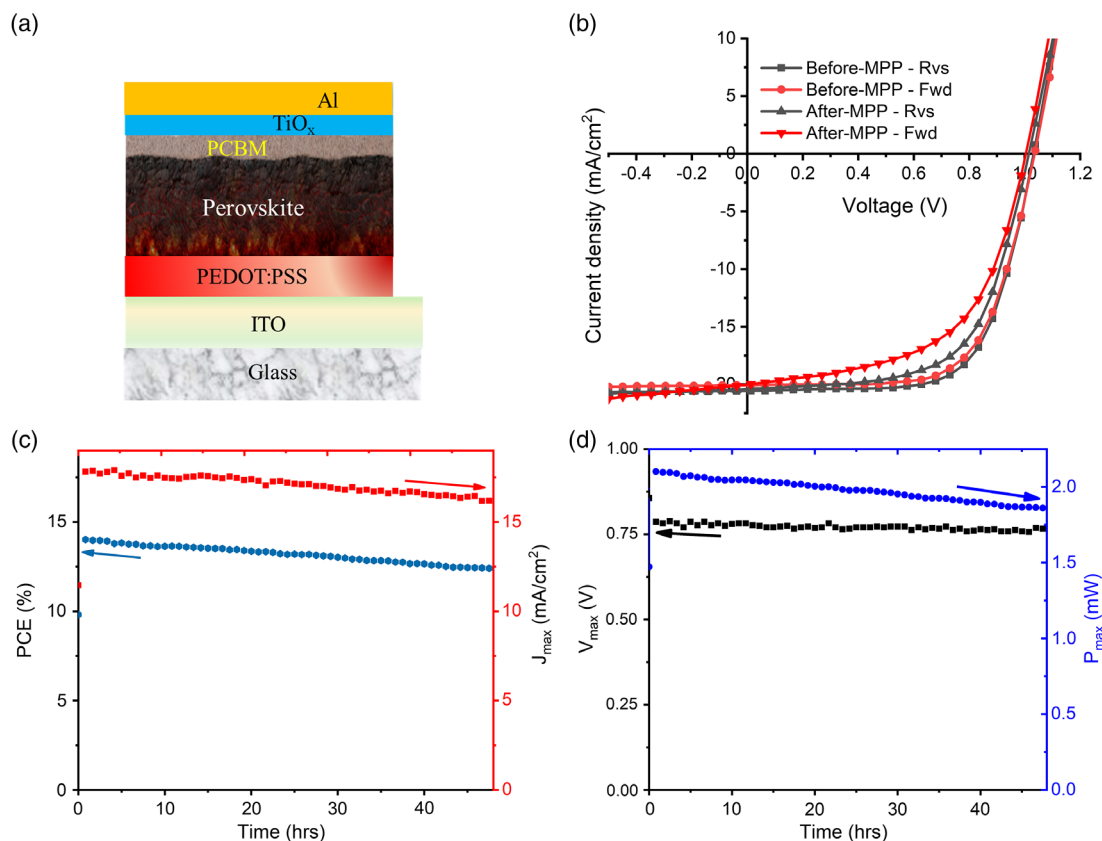


**Figure 1.** a) Schematic diagram of the PSC used. b) Photoinduced current density–voltage ($J$–$V$) characteristics of PSC before (black) and after (red) MPP tracking under AM1.5 solar spectrum (100 mW cm$^{-2}$ light intensity) illumination. MPP tracking of an encapsulated PSC; c) steady-state PCE (hexagon) and current density at maximum power ($J_{max}$, cube), and d) voltage at maximum power ($V_{max}$, cube) and maximum power ($P_{max}$, sphere) under 100 mW cm$^{-2}$ light intensity continuous illumination in ambient air.

corresponding voltage at MPP ($V_{max}$) are shown Figure 1d. The device degraded by about 8% from its initial photovoltaic properties (PCE, $J_{max}$, and $V_{max}$) after continuous operation for 48 h.

## 2.1. Electrical Impedance Spectroscopy Response

EIS is a nondestructive electrical characterization technique used to investigate the electrochemical dynamics in the bulk and/or interfaces of different materials with both electronic and ionic behaviors, such as solar cells, different electrochemical electrodes, batteries, and fuel cells. EIS measures the resistive and capacitive behavior of an electrochemical system by applying an alternating current (AC) potential at different frequencies and measuring the alternating current response through the cell. EIS can be applied in combination with light illumination to characterize solar cells under operation conditions. The different physical processes occurring in the device will appear in the EIS responses at different characteristic frequencies.[20]

In this study, the EIS response of the device was measured before and after the MPP-tracking experiment. The EIS was recorded at short-circuit conditions with 10 mV AC voltage under different light-emitting diode (LED) light ($\lambda = 590$ nm) intensities (3.2, 6.4, and 8 mW cm$^{-2}$) illumination in the frequency range between 1 MHz and 0.02 Hz. The impedance characteristics of the PSC presented in Nyquist plots show two semicircles in two distinct frequency regions which represent different processes in the device (**Figure 2**a).[21–24] Figure 2b shows the corresponding Bode plots of the EIS characteristics.

An equivalent-circuit model with two time constant suggested by Garcia-Belmonte and coworkers[25,26] is applied to interpret the EIS responses (Figure 2c). The circuit is a combination of the external series resistance ($R_1$) including contacts resistance, wire resistance, and sheet resistance of the electrode, two non-ideal capacitive element called constant-phase element (CPE1 and CPE2) and two resistive ($R_2$ and $R_3$) elements. The impedance of a constant-phase element (CPE) is given by

$$Z_{CPE} = \frac{1}{T(j\omega)^P} \tag{1}$$

where $T$ is a constant with the unit F cm$^{-2}$, and $P$ is related to the angle purity. The capacitive element, CPE1 represents the non-ideal geometric capacitance and is associated with the dielectric response of the perovskite layer which dominates the capacitive response in the high-frequency region (>1 kHz) of the spectra. The second capacitive element, CPE2 is a low-frequency response (≤1 Hz) related to the surface charge accumulation at the interfaces of the solar cell. The resistance, $R_2$ is coupled with CPE1 and associated with the charge transport resistance of the bulk perovskite. It is also influenced by the transport resistance of the ETL.[27] The low-frequency resistance, $R_3$ is associated with many processes like surface resistance, accumulation resistance at interfaces, and slow processes like ion diffusion and trap-mediated charge recombination resistance in the bulk.[25,28]

The fitting parameters of each circuit element for the EIS response under 8 mW cm$^{-2}$ light illumination are shown in **Table 1**. The EIS characteristics show that after 48 h of continuous operation the transport resistance ($R_2$) increases and the CPE1, related to the dielectric properties of the perovskite material, decreases by about 4 nF. The low-frequency CPE2 increases by about 60 mF, whereas the interface-related resistance ($R_3$) shows negligible change. The increase CPE2 could be related to ions and electrons accumulation at interfaces during the
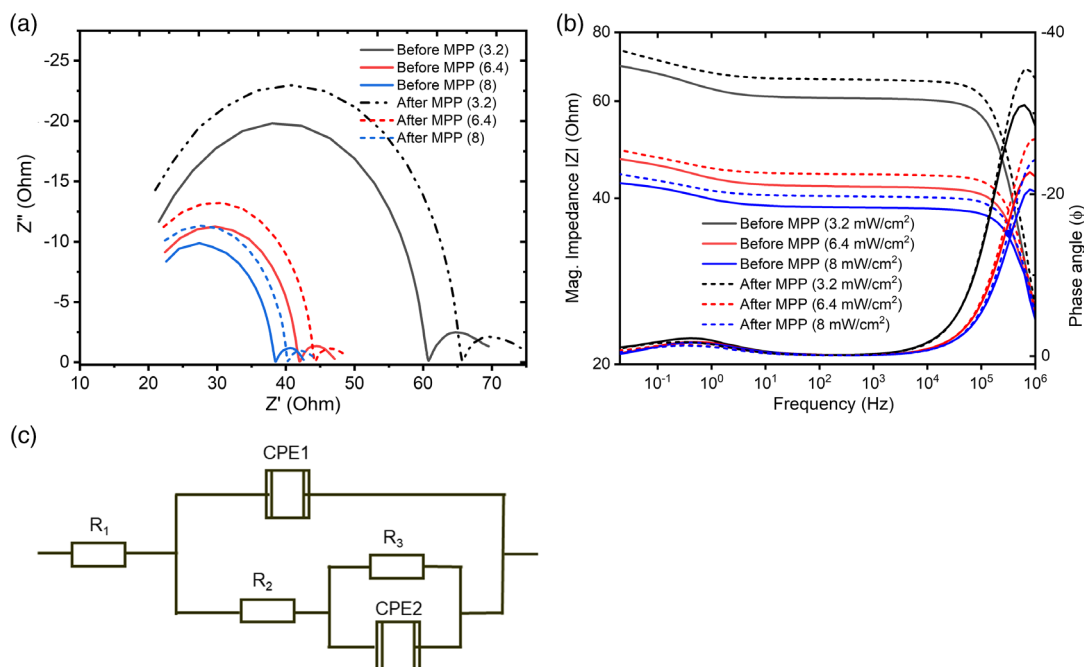


**Figure 2.** a) The Nyquist and b) Bode plots of EIS characteristics of the device before (solid lines) and after (dash lines) MPP tracking, measured at short-circuit condition with 10 mV AC voltage and under different light intensities (3.2, 6.4, and 8 mW cm$^{-2}$) LED light ($\lambda = 590$ nm) illumination. c) Equivalent circuit model for the solar cell.

**Table 1.** Equivalent circuit fitting parameters; series resistance ($R_1$), transfer resistance ($R_2$), CPE1 corresponding to the bulk, resistance related to interface ($R_3$) and interface-related CPE2, extracted from the fitting of EIS response of PSC before and after MPP tracking measured under 8 mW cm$^{-2}$ LED light ($\lambda = 590$ nm) illumination.

| Measurement | $R_1$ [$\Omega$] | $R_2$ [$\Omega$] | $R_3$ [$\Omega$] | CPE1 | | CPE2 | |
|---|---|---|---|---|---|---|---|
| | | | | $T$ [F] | Phase | $T$ [F] | Phase |
| Before MPP | 17.5 | 20.9 | 4.3 | 2.66E-08 | 0.96 | 0.12 | 0.66 |
| After MPP | 16.5 | 23.7 | 4.6 | 2.26E-08 | 0.98 | 0.18 | 0.55 |

MPP tracking. This will increase the ion diffusion and accumulation resistance. In contrast, the trap-mediated bulk recombination resistance decreases when more traps are formed in the bulk and the overall effect on the R3 is small.

In the EIS response of the devices before and after MPP tracking (Figure 2), the semicircle arc for high- and low-frequency regions shrinks as the LED light intensity increases. The electrical properties of the device extracted from the EIS response, under different LED light intensities are shown in **Figure 3**. The two resistive elements ($R_2$ and $R_3$) decrease as the illumination intensity increases, whereas the capacitive element associated with the interface (CPE2) increases with illumination intensity. As the light intensity increases the photogenerated

charge density increases, and therefore the conductivity and dielectric constant of the perovskite increases which leads to a reduction of $R_2$.[23,29–31] Similarly, the decrease in $R_3$ could be related to the increase in electronic and ionic migration and recombination kinetics with illumination light intensity.[25,32] The corresponding angular frequencies (where the imaginary impedance is maximum) shift to higher frequency as the illumination intensity increases, which indicates that the charge carrier lifetime decreases.

The bulk-capacitor (Figure 3a) decreases after the MPP tracking, and the differences are becoming larger at lower light intensities (1.6 mW cm$^{-2}$). The charge transport resistance ($R_2$) increases after MPP tracking (Figure 3b). This indicates that charge carriers are trapped and the charge transport process is hindered. As mentioned earlier, the interfacial charge impedance ($R_3$) does not change significantly (Figure 3c). This could indicate that the impedance across the charge transporting layers does not change within the testing period. However, the interfacial capacitive element (CPE2) increases after MPP tracking (Figure 3d). This indicates that the accumulation of electronic and ionic charge carriers at the interface increases,[23,26,27] suggesting ionic migration to the interfaces leaving behind defect states in the bulk of the perovskite.[27,33] This could explain the increase in the observed $J–V$ hysteresis.

Analogously, the EIS characteristics of the MAPbI$_{3-x}$Cl$_x$ PSC with a BCP ETL interlayer (Figure S1c,d, Supporting
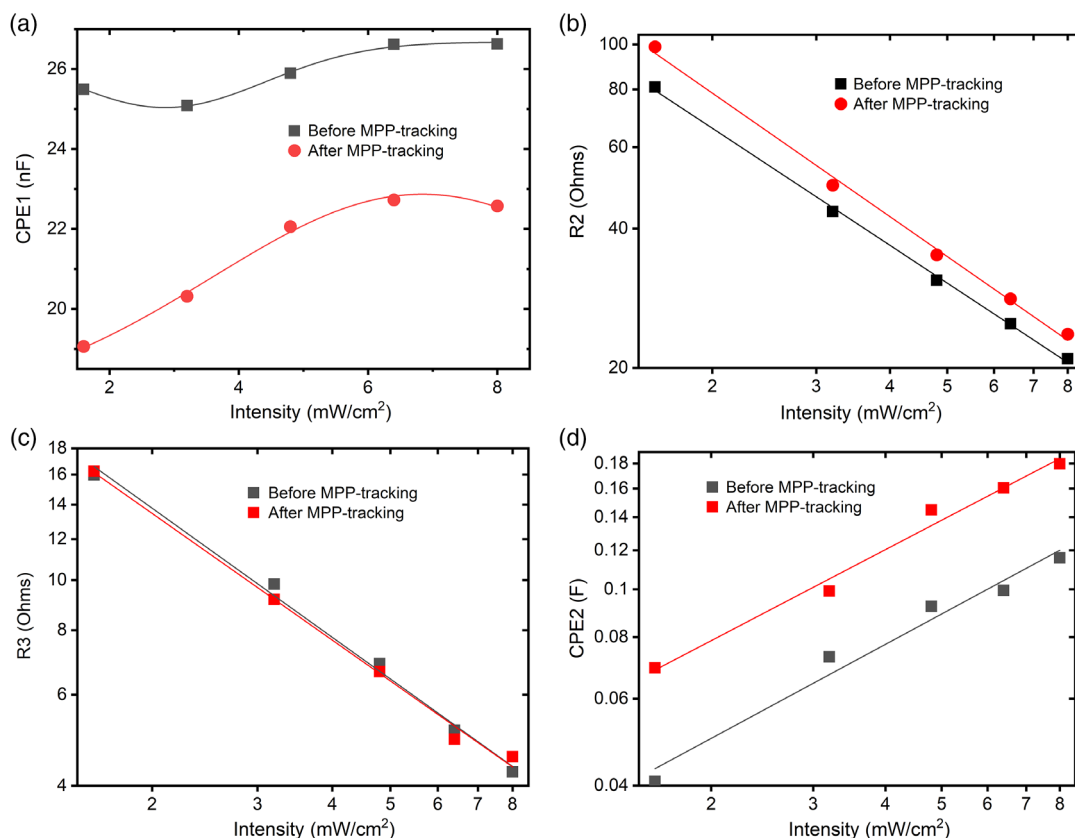


**Figure 3.** Comparative electronic properties of the PSCs before (cube) and after (sphere) MPP tracking: a) bulk-CEP1, b) charge transport resistance ($R_2$), c) interfacial recombination resistance ($R_3$), and d) interfacial CEP2 under illumination of 1.6, 3.2, 4.8, 6.4, and 8 mW cm$^{-2}$ LED light ($\lambda = 590$ nm) intensities.

Information) show that the charge transport resistance increases under continuous operation, whereas the low frequency, slowly moving species and interfacial processes resistance, shows negligible change.

## 2.2. Intensity-Modulated Photovoltage Spectroscopy

Intensity-modulated photovoltage spectroscopy (IMVS) is a light intensity-modulated impedance technique used to characterize the recombination dynamics in PSCs under open-circuit conditions. The IMVS response involves the measurement of frequency-dependent transfer functions between the modulated input photon-flux function ($\bar{\Phi}$) and measured modulated photovoltage output ($\tilde{U}_{photo}$).[34]

$$H_{IMVS}(\omega) = \frac{\tilde{U}_{photo}}{\eta q \bar{\Phi}} = \frac{\tilde{U}_{photo}}{\bar{\Phi}} e^{i\varphi} \qquad (2)$$

where $\eta$ is the quantum efficiency for charge generation, $q$ is the elementary charge, and $\varphi$ is the phase angle. The IMVS transfer function ($H_{IMVS}$) has units of $\Omega\,cm^2$ which shows IMVS can be related to the impedance.

The IMVS response of the same device used for EIS measurement was recorded at open-circuit conditions, under LED light ($\lambda = 590\,nm$) illumination with 10% light-intensity perturbation in the frequency range between 1 MHz and 20 mHz. **Figure 4** shows the IMVS characteristics of the device measured before and after the MPP tracking. Figure 4a shows the Nyquist plot, and Figure 4b shows the imaginary transfer function ($H''$) versus frequency recorded at different light intensities. The high-frequency response in the IMVS spectrum represents the dielectric property of the bulk perovskite layer, associated with the parallel combination of the recombination resistance. The second semicircle appearing at low-frequency is associated with the charge accumulation at the interfaces. The continuous operation led to a decrease in the diameter of the high-frequency semicircle, suggesting a reduction of the charge recombination resistance of the solar cell.[23,34] This is in a good agreement with the EIS response which indicates the charge transport resistance increases during continuous operation.

To extract the recombination time constants, the IMVS response of the device was measured under different LED light ($\lambda = 590\,nm$) intensities (1.6, 3.2, 4.8, 6.4, 8 mW cm$^{-2}$) with identical modulation amplitude and frequency region. The open-circuit voltage of the device shows to decrease after 48 h of continuous operation, under different light intensity illuminations (Figure 4c). The intensity ($I_o$) dependence of the $V_{OC}$ is given by
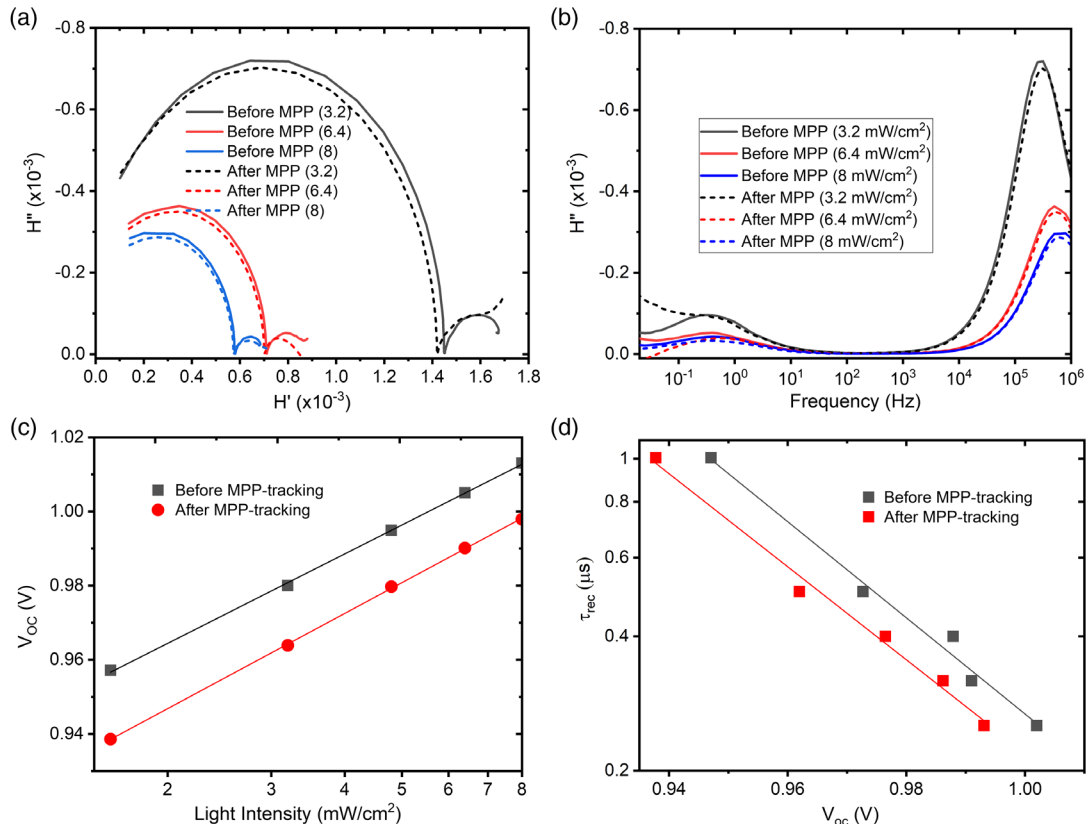


**Figure 4.** a) Nyquist and b) imaginary transfer function ($H''$) of IMVS characteristics of the device before (solid lines) and after (broken lines) the MPP-tracking measurement, under 3.2, 6.4, and 8 mW cm$^{-2}$ LED light illumination with 10% light intensity modulation amplitude. c) Open-circuit voltage ($V_{oc}$), and the time constants of IMVS response of the device before (cube) and after (sphere) under different intensities (1.6, 3.2, 4.8, 6.4, and 8 mW cm$^{-2}$) LED light illumination with identical modulation amplitude extracted from d) high-frequency region.

$$\frac{\partial V_{OC}}{\partial \ln I_o} = \frac{mk_B T}{q} \quad (3)$$

where $k_B$ is the Boltzmann constant, $T$ is temperature, and $q$ is elementary charge. The nonideal behavior of recombination ($m$) is related to the slope of the curves ($m_d = \frac{q}{k_B T}$ slope). The $m$ value of the device increases from 1.35 to 1.44 after continuous operation for 48 h, indicating the deviation from band-to-band recombination which could indicate the increase in trap-assisted recombination processes.[23]

The charge carrier recombination time constants ($\tau_{IMVS}$) of the PSC before and after the MPP tracking as a function of the $V_{OC}$ are extracted in the high-frequency region (Figure 4d). In IMVS, the critical frequency corresponding to the maximum of $H''$ at high frequency, is related to critical time by $f_c = \frac{1}{2\pi\tau_c}$.[21] The device recombination time constants in the high-frequency region show similar dependency trends on the light intensity before and after the MPP tracking. But at a given intensity, the device $V_{OC}$ decreases after operation which is in good agreement with the reduced recombination resistance illustrated in the Nyquist plots of the IMVS results (Figure 4a). Consequently, at a given $V_{OC}$, the high-frequency $\tau_{rec}$ shows the reduction of the recombination time constant. This suggests that the reduction of the device photovoltaic properties upon continuous operation is mainly related to the changes in the bulk of the photoactive perovskite film which is in good agreement with the EIS response. The IMVS characteristics of the PSC with BCP interlayer (see Figure S2a,b and Figure S3a,b, Supporting Information) show analogous trend with the response observed for the device with a $TiO_x$ interlayer.

## 2.3. Capacitance–Voltage

The EIS characteristics of the PSC show that the interface-related capacitive behavior increases under continuous operation, suggesting an increase in ion accumulation at the interfaces upon continuous operation. This could be explained by ion migration from the bulk to the interfaces leaving behind defect-states in the bulk. To confirm the change of defect-state densities in the photoactive layer, a Mott–Schottky analysis was performed using the $C–V$ response of the device. **Figure 5**a,b shows the $J–V$ characteristics and Mott–Schottky plots of $MAPbI_{3-x}Cl_x$ PSC measured at 10 kHz with 10 mV AC voltage (−0.5 to 1.2 V bias range) under dark conditions, before and after MPP tracking. The $J–V$ curves show s-shaped characteristic after 90 and 290 h MPP tracking. This might be related to the light soaking, charge trapping/detrapping processes and ion accumulation at the interfaces.[35–37]

The Mott–Schottky plots comprise two distinct regions which are related to the geometrical capacitance ($C_g$) and accumulation capacitance ($C_s$), as shown in Figure 5b.[38,39] The Mott–Schottky plot of the studied solar cells do not show a distinguishable depletion layer capacitance ($C_{dl}$) region. This could be related to the fact that layers containing less defects (films with good crystalline quality) cannot yield distinguishable $C_{dl}$ region in the Mott–Schottky plot representation.[38] This suggests that studied devices had good films quality and a low intrinsic defect density. $C_g$ represents the constant plateau $C^{-2}$ ($V$) response at low applied biases. It depends on the layer thickness, dielectric properties of the perovskite film, and vacuum permittivity. While the response in the forward bias near and/or above the built-in voltage corresponds to $C_s$, which is a capacitance caused by electrode polarization phenomena and charge accumulation at the interfaces. The built-in potential and defect density could be obtained from the voltage intercepts and from the slope, respectively, by fitting the $C^{-2}$ with respect to the bias in the $C_s$ region. In the Mott–Schottky plot, $C^{-2}$ and $V$ are related by[38–41]

$$\frac{1}{C^2} = \frac{-2(V - V_{bi})}{\varepsilon\varepsilon_\circ q A^2 N} \quad (4)$$

where $N$ is the defect density in the perovskite film, $q$ is the elementary charge, $\varepsilon$ is the dielectric constant of the perovskite ($\approx 32.5$), $A$ is the device area (0.15 cm$^2$ for both the sample and control cells), $V_{bi}$ is the built in voltage, and $\varepsilon_o$ is vacuum permittivity. The trap density in the device is extracted from the slope of a Mott–Schottky plot (i.e., slope $= \frac{-2}{\varepsilon\varepsilon_\circ q A^2 N_t}$) in the
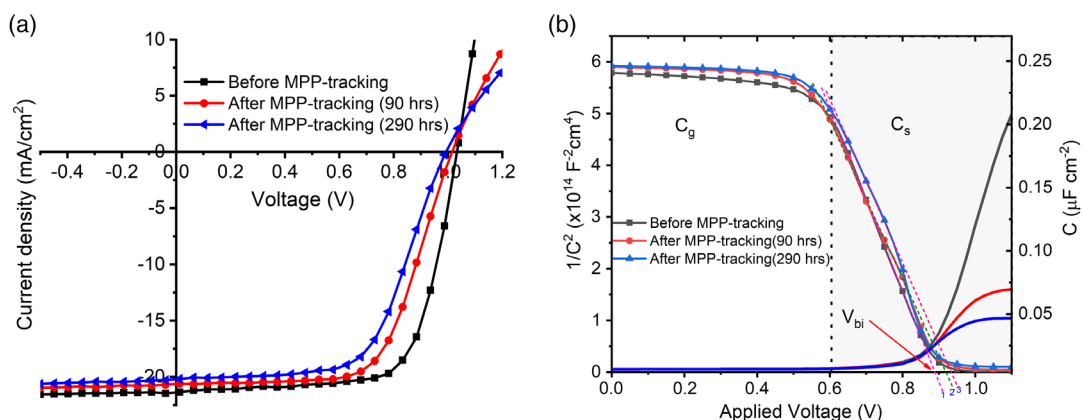


**Figure 5.** a) $J–V$ characteristics of $MAPbI_{3-x}Cl_x$ PSC under AM1.5 solar spectrum (1 sun) illumination before (cube) and after 90 h (sphere) and 290 h (triangle) MPP tracking. b) $C–V$ characteristics and Mott–Schottky plots ($C^{-2}$ vs $V$) of the same PSC with active area of 0.15 cm$^2$, before and after MPP tracking measured at 10 kHz with 10 mV AC voltage oscillation in forward bias (applied voltage range from −0.5 to 1.2 V) under dark condition. The fitting for curves before MPP tracking, after MPP tracking for 90 and 290 h are labeled as 1, 2, and 3, respectively.

depletion region ($V < V_{bi}$). The trap density ($N_t$) of the device increases from $\approx 2.6 \times 10^{15}\,cm^{-3}$ to around $2.8 \times 10^{15}\,cm^{-3}$ after 90 h under continuous operation, which was further increased to $3 \times 10^{15}\,cm^{-3}$ after 290 h continuous operation. Analogous trap-density trend was observed for similar devices after continuous operation for 30 and 90 h (see Figure S4a,b, Supporting Information). The changes in the defect density extracted from Mott–Schottky analysis are rather small. However, the capacitance and resistance measurements suggest quite significant changes of the trap density upon MPP tracking.[25,29] This discrepancy is not understood at the moment, but may be related to the different measurement conditions applied in the EIS (under illumination) and $C–V$ (dark) experiments. However, this slight change suggests the trap-states density increases with time under MPP tracking, leading to a decrease in device performance. This is in agreement with the increase in charge transport impedance and the interface capacitance, which suggests the ion migration to the interface leaving trap states in the perovskite film. From this, we could understand that the changes in the Mott–Schottky plots and device performance under continuous operation is predominantly related to the changes in the photoactive perovskite layer as well as the ion accumulation at the interfaces.

## 3. Conclusion

In summary, the electrical and ionic dynamics across the bulk and interfaces of the PSCs were characterized before and after MPP tracking, using an electrochemical impedance. EIS results show that the device charge transport resistance and interfacial capacitance associated with charge accumulation are increased after continuous operation. This suggests the ion migration from the photoactive perovskite layer to the charge selective layers leaving defects in the bulk. Furthermore, IMVS characteristics illustrate a decrease in charge recombination resistance, indicating the formation of more trap states in the device under continuous operation. The increase in the interfacial charge carrier recombination time constant under continuous operation indicates that the average charge carrier lifetime of the charges generated in the device is increased. This could be associated with the accumulation of electronic and ionic charge carriers at the interfaces. Moreover, $C–V$ characteristics and Mott–Schottky analysis of the solar cells show a consecutive increase in the trap-state density by about 8% after 90 h and 15% after 290 h continuous operation. This could be due to ionic migration to the interfaces leaving behind defect states in the bulk of the perovskite under MPP tracking. From this study, we can conclude that the decay of the device performance upon continuous operation is mainly related to the changes in the bulk of the photoactive perovskite film and ion accumulation at the interfaces.

This study suggests that to reduce ion migration-induced device decaying, "better" perovskite semiconductors and smarter interface engineering are required. "Better" perovskite semiconductors could be achieved through a careful understanding of the physics and chemistry of the materials, and precise compositional and process designing.

## 4. Experimental Section

*Materials*: Patterned indium tin oxide (ITO)-coated glass substrates (15 $\Omega\,cm^{-2}$), lead iodide (PbI$_2$, Sigma Aldrich, 99.9%), lead chloride (PbCl$_2$, Sigma Aldrich, 99.9%), [6,6]-phenyl-C$_{61}$-butyric acid methyl ester (PCBM, Solenne BV), poly(3,4-ethylenedioxythiophene) polystyrene sulfonate (PEDOT:PSS, Clevios PH 1000), Zonyl FS-300 fluorosurfactant (40% in H$_2$O, Fluka), methylammonium iodide (MAI), isopropanol (IPA), N,N-dimethylformamide (DMF, anhydrous, Sigma Aldrich), dimethylsulfoxide (DMSO, Anal. R. VWR chemicals, 99.5%), acetone, ethanol, and acetylacetone (CH$_3$COCH$_2$COCH$_3$, Sigma Aldrich, $\geq$99%) were used as-purchased. TiO$_x$ sol–gel was synthesized following the procedure reported by Park et al.[42] and used as an interlayer between PCBM and Al back electrode.

*Device Fabrication*: ITO-coated glass substrates were sequentially cleaned in acetone, detergent, deionized water, and IPA. Then, PEDOT:PSS (Clevious PH1000) was spin-coated on top of ITO at 1500 rpm for 45 s and dried at 120 °C for 15 min which was followed by IPA washing via spin coating at 4000 rpm for 15 s. The substrates were heated again at 120 °C for 15 min. MAPbI$_{3-x}$Cl$_x$ perovskite solution was prepared by dissolving PbI$_2$, PbCl$_2$, and MAI in defined molar ratio (1:1:4 mol. ratio, respectively) in DMF containing 10 vol% acetylacetone additive to get 0.88 M total concentration. After the PEDOT:PSS films were cooled to room temperature, the MAPbI$_{3-x}$Cl$_x$ perovskite solution was spin coated at 1000 rpm for 17 s and 2000 rpm for 5 s. The films' formation was completed by annealing at 115 °C for about 25 min. The films were then cooled to room temperature, and 2% (wt/wt) of PCBM solution dissolved in a mixture of chlorobenzene and chloroform (50:50 volume ratio) was spin-coated on top of the poly(vinyl siloxane) film. Then, TiO$_x$ sol–gel was spin coated on top of PCBM at 5000 rpm for 30 s and annealed at 110 °C for 10 min. Finally, device fabrication was finalized by thermal evaporation of 110 nm Al back electrode.

*Characterization*: The characteristic photocurrent density–photovoltage response of devices before and after MPP tracking was measured with a Keithley-2401 source meter. A LOT-QD solar simulator with a 1600 W xenon lamp providing AM1.5 global spectrum was used for irradiation. The intensity of the solar simulator was adjusted using a calibrated silicon reference diode.

MPP tracking measurement of an encapsulated solar cell was carried out in ambient air under 1 sun illumination with a Keithley-2400 source meter, and ATLAS solar simulator (SoTest 1200) was used as a light source. A continuous ventilation was applied to keep the temperature around the sample low.

EIS characterization of PSCs was carried out, before and after MPP-tracking measurement was done, under LED light ($\lambda = 590$ nm) illumination in the frequency range of 1 MHz–0.02 Hz using a SolarLab XM-Potentiostat/Galvanostat setup equipped with ModuLab XM PhotoEchem software.

A Novocontrol impedance spectrometer was used to measure the capacitance–applied voltage ($C–V$) response of PSCs to evaluate the trap density. The solar cells were connected to the impedance via the four-wire impedance test interface system in which the bottom contact was connected to the high current interface and the top (cathodic) contact was connected to the low current port. The instrument was equipped with WinDETA software to control the instrument and to carry out data analysis. The sample specifications regarding the active area and thickness were set to 0.15 cm$^2$ and 70 nm, respectively, to eliminate the effect of spray capacitance. Frequency of 10 kHz and AC voltage of 10 mV were filled in the initial and final conditions. Then the applied direct current (DC) voltage was set in the range from $-0.5$ to 1.5 V (forward bias) with 0.025 V steps. The $C–V$ response of the devices was measured under dark conditions, and from which the $C–V$ measurement and Mott–Schottky analysis were done.

## Supporting Information

Supporting Information is available from the Wiley Online Library or from the author.

**ADVANCED
SCIENCE NEWS**

www.advancedsciencenews.com

**pss**a
physica status solidi

www.pss-a.com

## Acknowledgements

## Conflict of Interest

The authors declare no conflict of interest.

## Keywords

[1] A. Kojima, K. Teshima, Y. Shirai, T. Miyasaka, *J. Am. Chem. Soc.* **2009**, *131*, 6050.

[2] NREL, Best Research Cell Efficiencies Chart, https://www.nrel.gov/pv/cell-efficiency.html, (accessed: August 2019).

[3] W. S. Yang, B.-W. Park, E. H. Jung, N. J. Jeon, Y. C. Kim, D. Uk Lee, S. S. Shin, J. Seo, E. K. Kim, J. H. Noh, S. Il Seok, *Science* **2017**, *356*, 1376.

[4] H.-S. Kim, C.-R. Lee, J.-H. Im, K.-B. Lee, T. Moehl, A. Marchioro, S.-J. Moon, R. Humphry-Baker, J.-H. Yum, J. E. Moser, M. Grätzel, N.-G. Park, *Sci. Rep.* **2012**, *2*, 1.

[5] H. Chen, F. I. Ye, W. Tang, J. He, M. Yin, Y. Wang, F. Xie, E. Bi, X. Yang, M. Grätzel, L. Han, *Nature* **2017**, *550*, 92.

[6] U. Krishnan, M. Kaur, M. Kumar, A. Kumar, *J. Photonics Energy* **2019**, *9*, 021001.

[7] L. Meng, J. You, Y. Yang, *Nat. Commun.* **2018**, *9*, 5265.

[8] W. Tress, K. Domanski, B. Carlsen, A. Agarwalla, E. A. Alharbi, M. Graetzel, A. Hagfeldt, *Nat. Energy* **2019**, *4*, 568.

[9] R. Fu, W. Zhou, Q. Li, Y. Zhao, D. Yu, Q. Zhao, *ChemNanoMat* **2019**, *5*, 253.

[10] F. A. Roghabadi, M. Alidaei, S. M. Mousavi, T. Ashjari, A. S. Tehrani, V. Ahmadi, S. M. Sadrameli, *J. Mater. Chem. A* **2019**, *7*, 5898.

[11] Z. Wang, D. P. McMeekin, N. Sakai, S. van Reenen, K. Wojciechowski, J. B. Patel, M. B. Johnston, H. J. Snaith, *Adv. Mater.* **2017**, *29*, 1604186.

[12] S. Yang, S. Chen, E. Mosconi, Y. Fang, X. Xiao, C. Wang, Y. Zhou, Z. Yu, J. Zhao, Y. Gao, F. De Angelis, J. Huang, *Science* **2019**, *365*, 473.

[13] S. Wang, H. Chen, J. Zhang, G. Xu, W. Chen, R. Xue, M. Zhang, Y. Li, Y. Li, *Adv. Mater.* **2019**, *31*, 1903691.

[14] B. C. Boyd, R. Cheacharoen, T. Leijtens, M. D. McGehee, *Chem. Rev.* **2019**, *119*, 3418.

[15] C. P. McMeekin, G. Sadoughi, W. Rehman, G. E. Eperon, M. Saliba, M. T. Hörantner, A. Haghighirad, N. Sakai, L. Korte, B. Rech, M. B. Johnston, L. M. Herz, H. J. Snaith, *Science* **2016**, *351*, 151.

[16] F. Bella, G. Griffini, J.-P. Correa-Baena, G. Saracco, M. Grätzel, A. Hagfeldt, S. Turri, C. Gerbaldi, *Science* **2016**, *354*, 203.

[17] W. Xu, L. Zheng, X. Zhang, Y. Cao, T. Meng, D. Wu, L. Liu, W. Hu, X. Gong, *Adv. Energy Mater.* **2018**, *9*, 1703178.

[18] X. Qin, Z. Zhao, Y. Wang, J. Wu, Q. Jiang, J. You, *J. Semicond.* **2017**, *38*, 011002.

[19] S. Heo, G. Seo, Y. Lee, M. Seol, S. H. Kim, D.-J. Yun, Y. Kim, K. Kim, J. Lee, J. Lee, W. S. Jeon, J. K. Shin, J. Park, D. Lee, M. K. Nazeeruddin, *Adv. Mater.* **2019**, *31*, 1805438.

[20] K. Adhitya, A. Alsulami, A. Buckley, R. C. Tozer, M. Grell, *IEEE J. Photovoltaics* **2015**, *5*, 1414.

[21] A. Pockett, G. E. Eperon, N. Sakai, H. Snaith, L. M. Peter, P. J. Cameron, *Phys. Chem. Chem. Phys.* **2017**, *19*, 5959.

[22] P. Wang, M. Ulfa, T. Pauporte, *J. Phys. Chem. C* **2018**, *122*, 1973.

[23] Q. Wang, *J. Phys. Chem. C* **2018**, *122*, 4822.

[24] A. R. Pascoe, N. W. Duffy, A. D. Scully, F. Huang, Y.-B. Cheng, *J. Phys. Chem. C* **2015**, *119*, 4444.

[25] I. Zarazua, G. Han, P. P. Boix, S. Mhaisalkar, F. Fabregat-Santiago, I. Mora-Seró, J. Bisquert, G. Garcia-Belmonte, *J. Phys. Chem. Lett.* **2016**, *7*, 5105.

[26] I. Zarazúa, S. Sidhik, T. Lopéz-Luke, D. Esparza, E. De la Rosa, J. Reyes-Gomez, I. Mora-Seró, G. Garcia-Belmonte, *J. Phys. Chem. Lett.* **2017**, *8*, 6073.

[27] A. Guerrero, G. Garcia-Belmonte, I. Mora-Sero, J. Bisquert, Y. S. Kang, T. J. Jacobsson, J. -P. Correa-Baena, A. Hagfeldt, *J. Phys. Chem. C* **2016**, *120*, 8023.

[28] X. Chen, Y. Shirai, M. Yanagida, K. Miyano, *J. Phys. Chem. C* **2019**, *123*, 3968.

[29] S. Ryu, D. C. Nguyen, N. Y. Ha, H. J. Park, Y. H. Ahn, J.-Y. Park, S. Lee, *Sci. Rep.* **2019**, *9*, 19846.

[30] J. Bisquert, *The Physics of Solar Cells: Perovskites, Organics, and Photovoltaic Fundamentals*, CRC Press, Taylor & Francis Group, LLC, Boca Raton, FL **2018**.

[31] D. J. Juarez-Perez, R. S. Sanchez, L. Badia, G. Garcia-Belmonte, Y. S. Kang, I. Mora-Sero, J. Bisquert, *J. Phys. Chem. Lett.* **2014**, *5*, 2390.

[32] G. Y. Kim, A. Senocrate, T.-Y. Yang, G. Gregori, M. Grätzel, J. Maier, *Nat. Mater.* **2018**, *17*, 445.

[33] H.-S. Kim, I.-H. Jang, N. Ahn, M. Choi, A. Guerrero, J. Bisquert, N.-G. Park, *J. Phys. Chem. Lett.* **2015**, *6*, 4633.

[34] A. Pockett, G. E. Eperon, T. Peltola, H. J. Snaith, A. Walker, L. M. Peter, P. J. Cameron, *J. Phys. Chem. C* **2015**, *119*, 3456.

[35] P. Lopez-Varo, J. A. Jiménez-Tejada, M. García-Rosell, S. Ravishankar, G. Garcia-Belmonte, J. Bisquert, O. Almora, *Adv. Energy Mater.* **2018**, *8*, 1702772.

[36] A. Sundqvist, O. J. Sandberg, M. Nyman, J.-H. Smått, R. Österbacka, *Adv. Energy Mater.* **2016**, *6*, 1502265.

[37] E. L. Unger, E. T. Hoke, C. D. Bailie, W. H. Nguyen, A. R. Bowring, T. Heumüller, M. G. Christoforo, M. D. McGehee, *Energy Environ. Sci.* **2014**, *7*, 3690.

[38] O. Almora, C. Aranda, E. Mas-Marza, G. Garcia-Belmonte, *Appl. Phys. Lett.* **2016**, *109*, 173903.

[39] P. Yadav, D. Prochowicz, M. Saliba, P. P. Boix, S. M. Zakeeruddin, M. Grätzel, *Crystals* **2017**, *7*, 252.

[40] I. J. Park, S. Seo, M. A. Park, S. Lee, D. H. Kim, K. Zhu, H. Shin, J. Y. Kim, *ACS Appl. Mater. Interfaces* **2017**, *9*, 41898.

[41] T. Bu, J. Li, F. Zheng, W. Chen, X. Wen, Z. Ku, Y. Peng, J. Zhong, Y.-B. Cheng, F. Huang, *Nat. Commun.* **2018**, *9*, 4609.

[42] S. H. Park, A. Roy, S. Beaupre, S. Cho, N. Coates, J. S. Moon, D. Moses, M. Leclerc, K. Lee, A. J. Heeger, *Nat. Photonics* **2009**, *3*, 297.